Self-assembling of Nonadditive Mixtures

Containing Patchy Particles with Tunable

Interactions

Isabela Quintela Matos¹ and Fernando Escobedo¹*

¹R. F. Smith School of Chemical and Biomolecular Engineering, Cornell University, Ithaca, New

York, USA

* Email: fe13@cornell.edu

ABSTRACT

Mixtures of nanoparticles (NPs) with hybridizing grafted DNA or DNA-like strands have been of

particular interest because of the tunable selectivity provided to the interactions between the NP

components. A richer self-assembly behavior would be accessible if these NP-NP interactions

could be designed to give nonadditive mixing (in analogy to the case of molecular components).

Nonadditive mixing occurs when the mixed state volume is smaller (negative) or larger (positive)

than the sum of the individual components' volumes. However, instances of non-additivity in

colloidal/NP mixtures are rare and systematic studies of such mixtures are non-existent. This work

focuses on patchy NPs whose patches (coarsely representing grafted hybridizing DNA strands)

not only encode selectivity across components but also impart a tunable nonadditivity by varying

1

their extent of protrusion. To guide the exploration of the relationship between phase behavior and nonadditivity for different patches' designs, the NP-NP potential of mean force (PMF) and a nonadditive parameter were first calculated. For one-patch NPs, different lamellar morphologies were predominantly observed. In contrast, for mixtures of two-patch NPs and (fully grafted) spherical particles, a rich phase behavior was found depending on patch-patch angle and degree of non-additivity, resulting in such phases as the gyroid, cylinder, honeycomb, and two-layered crystal. Our results also show that both a minimum positive nonadditivity and multivalent interactions are necessary for the formation of ordered network mesophases in the class of models studied.

I. INTRODUCTION

Colloidal particle shapes and particle-particle interactions can be designed to produce numerous self-assembled ordered phases. ¹⁻⁹ For example, interparticle interactions have been deployed that mimic those of block copolymers, i.e., particles with connected but chemically incompatible domains, as these would offer structural versatility and a broad range of base-chemistries and feature scales. ^{10,11} In a recent study, a single component system of "two-block" Janus particles with staggered rectangular patches was found to nucleate into the single gyroid phase in a Monte Carlo simulation study. ¹² Another physical method to generate diverse phase behavior in colloidal particles is to graft nanoparticles (NPs) with complementary DNA strands to enact preferential attractions between select mixture components. ^{13–17} Recent experiments and simulations have demonstrated that mixtures of DNA-modified NPs and much smaller NPs (which represent mobile "electron equivalents") can assemble into hexagonal, cylinder, and triple double-gyroid phases. ¹⁸

A model proposed by Kumar-Molinero which implicitly encoded for positive nonadditivity in the inter-particle potential of colloidal particles led to the formation of a wide variety of novel mesophases, including some typically associated with block copolymers (like the lamellar, gyroid, and hexagonal). 19,20 The Kumar-Molinero (KM) model uses a mixing rule where the characteristic length "o" of the contact distance between two particles A and B differs from the arithmetic average of the characteristic contact lengths for A pairs and B pairs, i.e., σ_{AB} = $((\sigma_{AA} + \sigma_{BB})/2 + \Delta)$ with $\Delta \neq 0$; for spherical sites, this corresponds to a departure of the socalled Lorentz's additivity rule. The KM is peculiar in that it combines a positive non-additivity $(\Delta > 0)$ with a preferential cross-species interaction energy parameter ($\varepsilon_{AB}/\varepsilon_{AA} > 1$), leading to a stronger attraction and longer distance of approach for unlike particles. This combination can favor the formation of ordered phases because the clustering of unlike pairs caused by their stronger contact energy generates a larger excluded volume than that for the clustering of like pairs, resulting in microphase segregation. This may explain why previous additive models have predicted a limited number of crystals and quasicrystals, 21-25 while models with non-additive potentials have led to the formation of microphase segregated phases like those associated with block copolymers. The effect of nonadditive mixing is also significant for molecular components, often leading to nontrivial phase behavior, such as azeotropy and eutecticity. Other examples of idealized non-additivity models that have been studied in the literature include the Widom-Rowlinson, ²⁶ the Asakura-Oosawa, ²⁷ and the nonadditive Holland models. ²⁸

In many of the previously mentioned nonadditive models, nonadditivity is artificially imposed in the mixing rule for the like and unlike interaction pairs, with no explicitly modeled NP functionalization or packing interaction that would physically generate the nonadditive behavior. However, there are physical examples where nonadditivity is realized, such as when using NPs

with suitably designed grafted patches, which present an anisotropy caused by the patches residing in either only one or multiple regions of the NP surfaces that influence how NPs interact and selfassembly. Janus particles having single patches, for instance, have previously been shown to assemble into micelles, tubes, and lamellae.²⁹⁻³² The influence of the number of patches per particle has also been studied, 1,33,34 with a primary interest in tetrahedrally arranged four-patch particles, since they can form the diamond crystalline phase, a sought-after structure for potential applications in photonic devices.^{35,36} Regarding the influence of nonadditivity on the assembly of these patchy particles, our group has recently shown that tetrahedrally grafted raised patches can kinetically enhance the formation of the diamond phase through increased positive nonadditivity.³⁷ Since the anisotropy of the NP patches could lead to an experimental realization of effective two-body potentials that approach the KM model, we chose two-component systems of spherical NP cores with nonadditive grafted patches as a platform to explore the correlation between patch design and phase behavior. These patches, which mimic preferential inter-species attractions (such as those generated by sequence-complementary grafted DNA or DNA-like strands of varying lengths), enable us to physically enact and control positive non-additivity through the decoration of NP surfaces with raised patches of differing heights and strengths of preferential attraction. Our model incorporates a highly coarse-grained representation of DNA hybridization and has tunable nonadditivity, allowing us to examine the influence on self-assembly of local nonadditivity (by varying patch height and softness of core-core interactions), multivalency (by varying the number

symmetry (by using patchy NPs for both or just one of the components). We used molecular dynamic simulations to investigate how such different system designs impacted the propensity to

of patches per NP), geometric frustration (by varying the angle between the patches), and mixture

form different micro-segregated mesophases.

The rest of the paper is organized as follows: Section II describes the Kumar Molinero Model, the interparticle potential models, simulation methods, and order parameters employed in this study; Sec. III contains the main results and associated analysis, and Sec. IV provides the concluding remarks and outlook for future work.

II. METHODS

A. Overview of the Kumar-Molinero Model

We explored the idea of using the potential of mean force (PMF) between two particles, either of the same type (A-A or B-B) or different types (A-B), as a guide to predict local positive nonadditivity in the many-particle system simulations. As for post-processing, we calculated the *micro or local nonadditivity* by using the diameters of the particles for like (σ_{AA}) and unlike (σ_{AB}) pairs.

Figure I(a), we compare the PMF between two Kumar Molinero (KM) particles to the radial distribution function of the mesophase formed (at a temperature of 300 K, pressure of 0 atm, and 74% of component A). These PMF calculations were performed using Monte Carlo simulations that place one of the particles at random positions and orientations within a given distance from a fixed particle following the protocol from Ref. ³⁸ The KM model uses a simplified Stillinger-Weber type of potential to model the intermolecular interactions between both like and unlike nanoparticles. The functional form of the potential is given in the Supplementary Information. To obtain the hexagonal cylinder phase and lamellar phases, we followed the simulation protocol detailed in the original article. ¹⁹ We see that the positive local nonadditivity associated with the Lorentz's rule shown in the PFM is realized in the contact distances between unlike and like particles (with $\sigma_{AB}/\sigma_{AA} = 1.15$). Figure 1 (b) shows the radial distribution function (RDF)

between the particles in the cylinder phase and the RDF between the individual components (A and B) before mixing happens (pre-mix). The RDF shows that upon mixing, neighboring like-type particles are pushed closer together from their pre-mix positions; this behavior arises from the stronger attraction between A-B particle pairs and the softness of the A-A and B-B interactions. Indeed, the energetic penalty of moving like particles closer together is small due to the softness of their potential and is compensated by the more favorable A-B contact energy; despite the longer A-B contacts, the more abundant A-A and B-B contacts lead to a smaller system volume upon assembly as seen in Figure 2. This volume decrease allows the efficient packing needed to enact as many A-B contacts as possible. This analysis also illustrates the limitations of the effective two-body NP-NP PMF in correlating with the phase assembly behavior that results from many-body interactions which are captured, albeit bluntly, by the excess volume of mixing Δν.

Despite the similarities in the types of phases that the KM model and typical diblock copolymers (BCPs) form, key differences exist in the mechanism of mesophase formation. The BCPs assemble into mesophases largely because the effective repulsion between the A and B blocks drives microphase segregation, with macrophase segregation precluded by the intrachain bonding of the A and B blocks; the system rearranges to decrease AB contacts and minimize interfacial area. In such systems, the main driving force to mesophase formation is hence energetic, with density changes being typically negligible, and entropic changes associated with polymer conformations having a secondary effect. In contrast, in the KM model, A-B contacts are energetically favorable but being more distant, they would tend to increase the system's volume and increase the free energy. Thus, the system rearranges to try to decrease its volume and consequently enhance packing entropy by favoring AA and BB contacts despite the associated energetic penalty and loss

of mixing entropy. This competition between energetics with mixing and packing entropy in the KM model results in microphase segregation and network phases akin to those formed by BCPs.

Table 1 sums up the comparison between the two systems. Based on this analysis, we defined three essential features that would allow us to map the KM model to the DNA functionalized NP model: A-B contact (energetic) selectivity, local nonadditivity, and core softness. While the directionality of the NP-NP interactions is absent in the spherically uniform KM model potentials, we incorporate it in our model as NP grafted patches to physically realize the local nonadditive attraction between unlike particles.

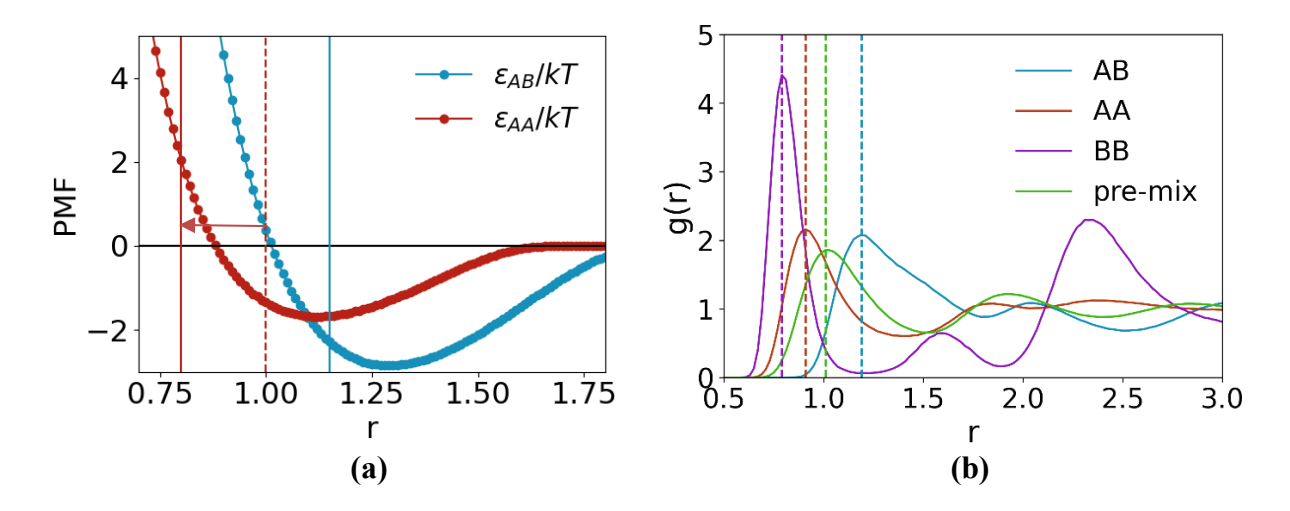


Figure 1: Sample KM model results. (a) Potential of mean force (PMF) in reduced units for values of the attraction ratio $\frac{\varepsilon_{AB}}{\varepsilon_{AA}} = 1.7$ and contact distance ratio $\frac{\sigma_{AB}}{\sigma_{AA}} = 1.15$ (b) Radial distribution function between particles of types A-B, A-A, and B-B in the hexagonal cylinder phase, and between particles before mixing. Phase formed at $x_A = 0.74$, $\frac{\varepsilon_{AB}}{\varepsilon_{AA}} = 1.7$, and $\frac{\sigma_{AB}}{\sigma_{AA}} = 1.15$.

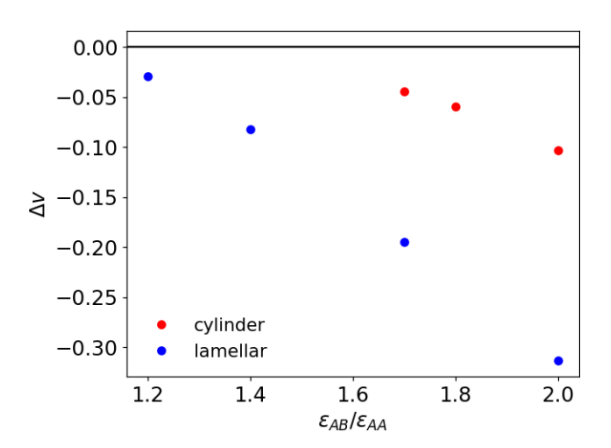


Figure 2: Volume difference between the mesophase and the pre-mix state of the individual components' phases normalized by the volume of the pre-mix state (Δv) for the KM model mesophase formed using $\frac{\sigma_{AB}}{\sigma_{AA}} = 1.15$ and different attraction parameter ratios at pressure = 0. More details about Δv calculation are given in the supplementary material.

Table 1: Comparison between driving forces for mesophase formation in diblock copolymers (BCP) and the KM model (Δ refers to changes upon mesophase formation).

Property	ВСР	KM model
ΔU	Effective repulsion between copolymer block chains A B	A B contacts energetically favorable
$\Delta(PV)$	Negligible variations in volume	Significant decrease in volume
TΔS	Small loss in mixing entropy and chain conformational entropic penalty to fit into domain geometry	Large loss in mixing entropy must be countered by an increase in packing entropy (AA and BB interactions)
ΔG	$<$ 0 by minimizing unfavorable A-B ΔU and conformational frustration	< 0 by maximizing favorable A-B ΔU and volume contraction (ΔPV) while minimizing ΔS loses

B. Mixtures of Grafted Nanoparticle Model

Based on the Lorentz's mixing rule, we first designed a coarse-grained nonadditive model for grafted NPs with one patch (1P). This model, summarized in Figure 3 (a), was intended to single out the effect of the local nonadditivity on phase behavior. The A-B selectivity (mimicking the effect of hybridization between grafted chains) is enacted by the attraction between complementary rigid central patches (CP). Each patch here is made of 19 identical Lennard-Jones central patch beads in a closed-packed hexagonal arrangement (see Fig. 3(a)), where $\sigma_P = 0.2$ and ε_{PAB}/kT being one of the parameters varied to map phase behavior. We also explored a model with flanking patches to enforce the directionality of the interactions whose PMFs are provided in the supplementary material. The unlike patches and core-patch interactions are purely repulsive (enacted through the Lennard Jones potential with a cutoff radius shifted to $2^{1/6}\sigma$). We kept the parameters for these interactions constant: $\sigma_{C-Patch} = 0.6$, $\sigma_{Patch} = 0.2$, $\sigma_{CAB} = 1$, $\varepsilon_{CAA} = 0.6$ $\varepsilon_{CBB} = \varepsilon_{C-Patch} = \varepsilon_{PA-PA} = \varepsilon_{PB-PB} = 1$. The like cores can be made to be purely repulsive or interact through the LJ potential and we explored both scenarios in our simulations. The degree of overlap between the like cores ($\sigma_{CAA} = \sigma_{CBB}$) can also be tuned to increase the local nonadditivity. A soft core would approximate a case where the core is loosely grafted with flexible chains, while the patches are densely grafted with longer, stiffer chains. The NPs are modeled as rigid bodies with all intramolecular interactions excluded. We note that the geometry and level of patch coarsegraining (as representing multi-chain grafting implicitly) adopted here would be most relevant to NP cores which are of intermediate size (say $40 \, \text{nm} < \sigma_{CAA} < 100 \, \text{nm}$) being significantly larger than the graft lengths,³⁹ and for relatively dense grafting densities that would allow smearing out the interactions of multiple individual grafts into effective soft beads.

Figure 4(a) shows the calculated the PMF (which captures the orientationally averaged NP-NP free energy at different distances) between two patchy NPs in vacuum. These PMF calculations followed the same protocol as that described in reference to Figure 1. Due to the stronger energetic complementary patch-patch interaction, the PMFs show a preferential contact at a longer distance between the unlike NP particles ($\sigma_{AB} = \sigma_{CAB} + 2H$) than the σ_{AA} of like particles which is equal to σ_{CAA} . To tune these relative contact distances, we change either σ_{CAA} or the height of the patch beads, where height (H) measures the extent of patch protrusion outside the core's surface; H ranged from zero (flat patch) to 0.2 ($\sigma_P = H$). A similar design was used before in exploring the relationship between nonadditivity and height of the patch for mixtures of four-patch particles.³⁷ The height of the patch is also directly associated with the preferential contact, i.e., NPs with more protruding patches (representing longer grafted chains) would have a larger σ_{AB} and r_{AB} . The patch coverage angle is fixed at $\Theta = 32^{\circ}$ for the one patch model, so that as the patch height increases by moving the patch beads away from the core center, so do the bead-bead distance and patch diameter (i.e., of the circumference that inscribes all the beads in one patch).

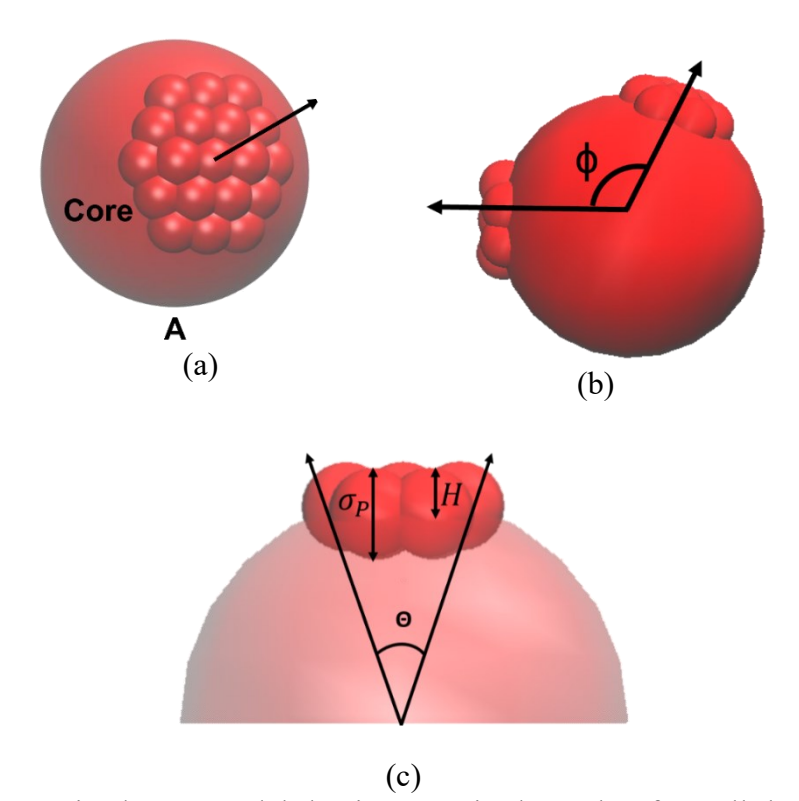


Figure 3: Coarse-grained NP model having a raised patch of small beads (representing complementary DNA grafts). The A-B selectivity (hybridization) is modeled using attractive, complementary patches. (a) One-patch model. (b) Two-patch model with the angle between patches (ϕ) highlighted. (c) Patch coverage angle (Θ) , patch bead diameter (σ_P) and height (H).

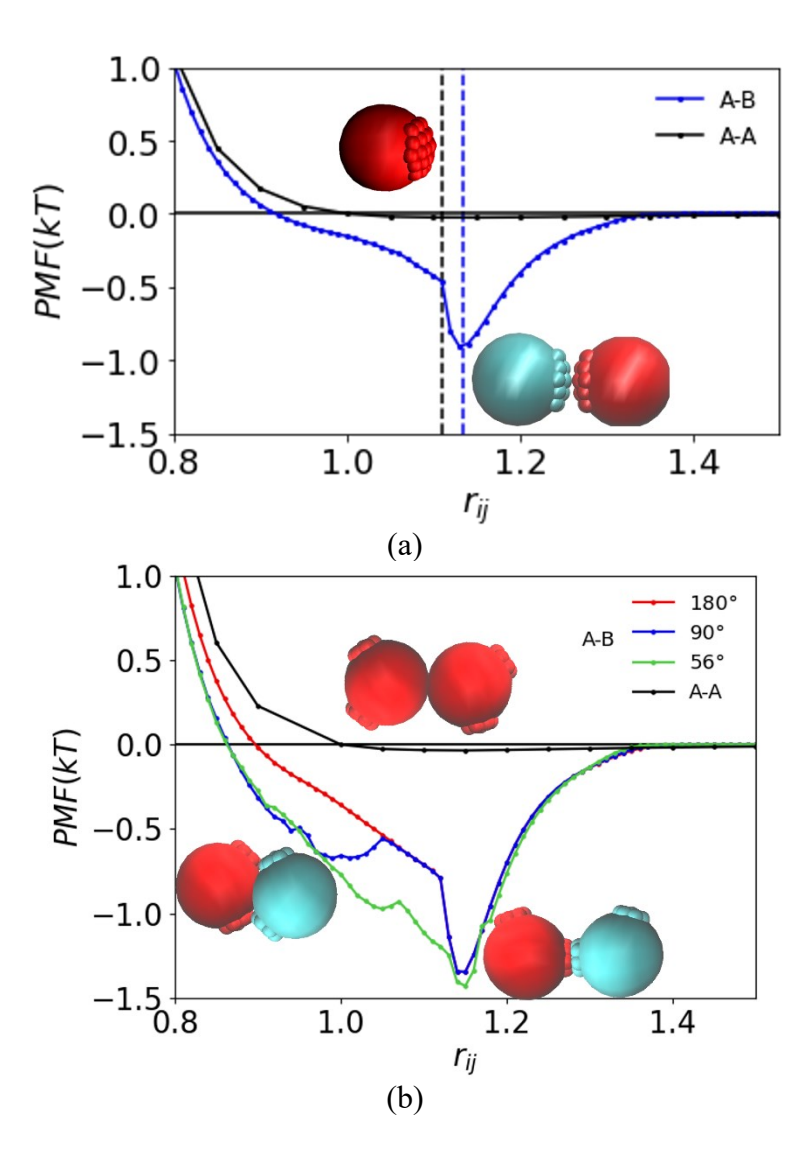


Figure 4: PMF (free energy) between two NPs in vacuum as a function of their center-to-center distance r_{ij} for: (a) One-patch NP, and (b) Two-patch NPs with different angles ϕ between the patches as marked in the legend. In (a) the vertical lines mark the minimum PMF value. The PMF values are divided by the total number of beads and curves were calculated using H = 0.075, $\sigma_{AB} = 1.15$, and $\sigma_{CAA} = 1$, with $\varepsilon_{PAB}/kT = 1.2$ for the one-patch particles and $\varepsilon_{PAB}/kT = 3$ for the remaining PMFs.

To probe the multivalence effect, we first explored NPs with two-patches (2P). Each patch now is made of 7 identical Lennard-Jones beads and the coverage angle is fixed at $\Theta = 30^{\circ}$, as shown in Figure 3 (b-c). The interactions among cores and central patches are equal to those described in

the previous paragraph. We also explored multiple angles (ϕ) between the patches, with some representative angles used in the PMF calculations of Figure 4 (b). We see that systems with higher ϕ values behave similarly to the one patch case because of the large distance between the patches, while systems with angles close to 90° have two wells that arise from the two favorable contact distances as illustrated in Fig. 4(b). The PMF for like particles was largely unaffected by the angles between the patches because their interaction potential is dominated by core-core contacts.

C. Binary Mixture of Patchy and (Non-patchy) Spherical Nanoparticles

NP patchiness creates anisotropic NP-NP interactions that may limit access to some of the mesophase morphologies which are accessible to the fully isotropic KM potential. To minimize this effect, we studied mixtures of densely grafted patchy NPs with longer stiffer chains (component A) and (non-patchy) loosely grafted NPs (component B) that are modeled as spheres, as depicted in Figure 5 (a). In this system, the patches will have attractive interactions with the implicit grafts all around the spherical particle B. Here, the patches are made of 7 identical Lennard-Jones central patch beads in a closed-packed hexagonal arrangement, and we define $\sigma_{AB} = \sigma_{CAB} + H$. All the other like interactions and modeling assumptions are the same as those for the mixture of patchy NPs described in the previous subsection. We also tuned the degree of overlap between the like cores and the spherical particles ($\sigma_{CAA} = \sigma_{CBB}$) to increase the local nonadditivity. We explored both, mixtures of one-patch NPs and the two-patch NPs as component A with spherical particles as component B. The PMFs for the mixtures with two-patch NPs are shown in Figure 5(b) for selected angles between the patches (ϕ). (The PMFs for the mixtures with one-patch NPs and additional PMF curves for different ϕ are available in the supplementary material). The effective AA and BB interactions (also shown in Fig. 5) are almost identical despite the presence of patches in the A particles. This happens because like-patches interactions are

repulsive and core-core contacts are most prevalent making the preferential distance of contact for like particles to be the same. A second potential well for angles in the region $80^{\circ} < \phi < 120^{\circ}$ occurs because this angular geometry allows the simultaneous interactions of two patches with the spherical particle.

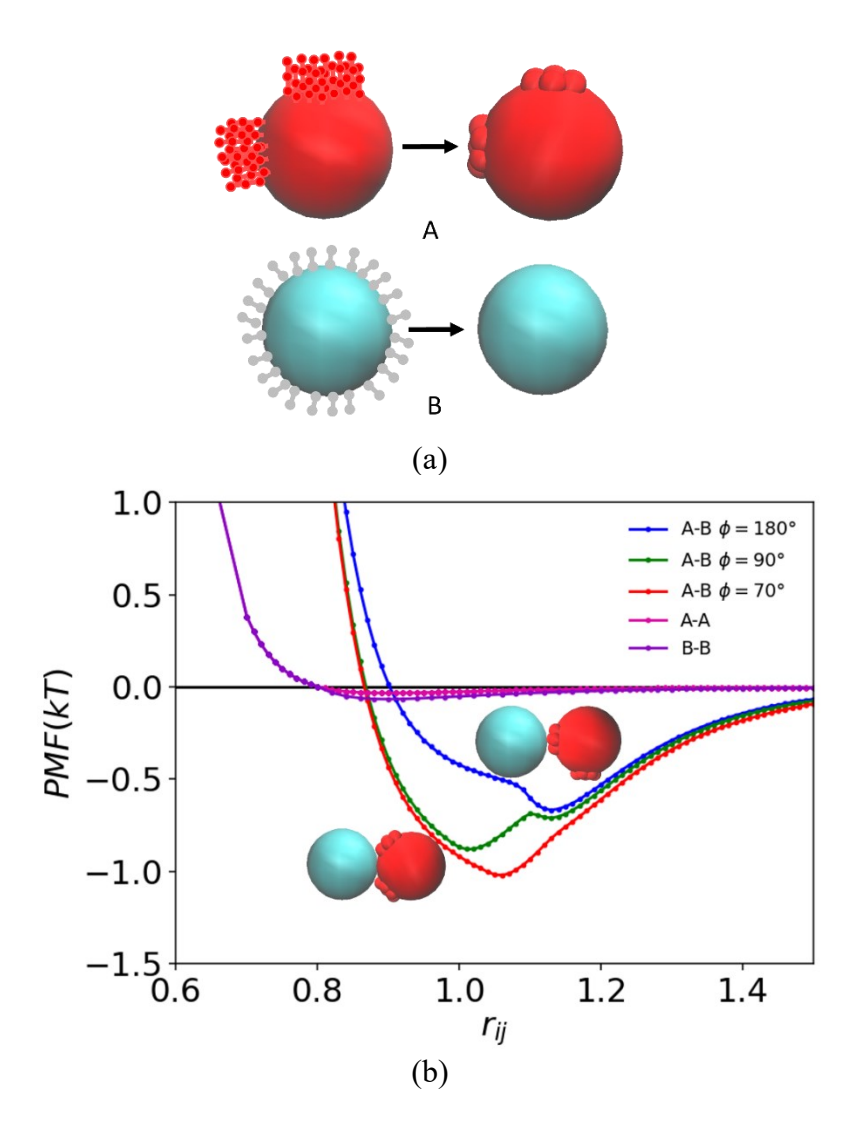


Figure 5: (a) Illustration of the implied grafted-chain \rightarrow patch coarse-graining for particles A and B. (b) PMF between two NPs in vacuum as a function of their distance r_{ij} for two-patch NPs (2P) with different angles between the patches (ϕ). The A-A PMF curves were similar for different values of ϕ ; the curve shown here corresponds to $\phi = 90^{\circ}$. The PMF values are divided by the total number of beads and curves were calculated using H = 0.08, $\sigma_{CAA} = \sigma_{BB} = 0.8$ and $\varepsilon_{PAB}/kT = 3$.

D. Simulation Details

After selecting the characteristics of our modes guided by the (two-NP) PMF results, we carried out Molecular dynamic simulations of many-NP systems to characterize their phase assembly behavior. The systems were simulated in the isothermal-isobaric (NPT) ensemble with rigid body dynamics and no intramolecular interactions using the LAMMPS software.⁴⁰ The systems sizes ranged from N = 1500 to 12000 with different compositions. The initial random configurations were cooled at a rate of 2×10^{-7} kT/step and constant pressure ($P^*=P\sigma^3/\varepsilon=0.5$) from a disordered state ($T^*=kT/\varepsilon=4$) until we observed the formation of an ordered structure, which typically occurred for $0.5 \le T^* \le 1.0$. The cooling runs consisted of 3×10^7 steps with a timestep of $\Delta t=0.001$. Thereafter, we equilibrated the system at the phase formation temperature for 1×10^7 steps. In some cases, we carried additional cycles of heating-cooling NPT runs to try to anneal out morphological defects.

E. Order Parameters

The phases were classified using structure factor calculations to identify the characteristic diffraction peaks of different ordered morphologies. These calculations were done using the center of mass of each NP. We also calculated the relative angle (θ) between neighboring spherical particles and the patches of the two-patch NPs. These θ angles are formed between the vectors connecting the center of mass of spherical particle i with patch 1 (r_{ij_1}) , and patch 2 (r_{ij_2}) of particle j.

III. RESULTS & DISCUSSION

A. Mixtures of Patchy Nanoparticles

Local nonadditivity is necessary but not sufficient to form network phases.

We first carried out simulations for one-patch NP with flanking patches and repulsive like-cores with $\sigma_{CAA}=1$ to evaluate the role of the Lorentz's nonadditivity in the self-assembly of the grated NPs. At the equimolar composition, we found that the system forms a thick lamellar phase or a thick layered crystal for a range of patch heights. For flat or "retracted" (non-raised) patches, the system forms thick layers of NPs for high values of the energetic attraction parameter. The latter is accompanied by the crystallization of the particles and, consequently, a decrease in the mobility of the particles. More details about the model with the flanking patches, snapshots of the phases formed, and a schematic phase diagram are provided in Figures S4 and S5 of the Supplementary Material. The thick lamellar transformed into macrophase-segregated domains when decreasing the attraction (ε_{PAB}/kT) between the unlike patches but crystallized when increasing it. We also calculated the distance between particles of the same type at the first peak of the radial distribution functions and observed that they stay at the distance corresponding to the well of the Lennard-Jones potential $(2^{1/6}\sigma)$ due to the harsh (r^{-12}) repulsion between cores. This characteristic of the system results in a negative local additive parameter for $\sigma_{AB} < 2^{1/6}\sigma_{AA}$ and positive local additive for $\sigma_{AB} > 2^{1/6}\sigma_{AA}$. Changing the mixture composition did not lead to other phases besides the lamellar phase; in particular, no trace of an ordered network phase, like the gyroid, was ever observed.

Softer core-core interactions and weaker directionality enable the formation of cylinders.

The appearance of cylinders-like structures in the one-patch model was associated with increasing the nonadditivity by decreasing σ_{CAA} to 0.8 for $x_A = 0.66$ and the removal of flanked

patches. Softening the core allowed for not only an increase in the local nonadditivity but also for more flexibility in the possible arrangements around the patches. As a comparison, we also explored the effect of increasing the patch-patch contact directionality and the fraction of the components with the model using flanked patches and observed that this generated a more restrictive one-on-one binding that favored lamellar phases (see Supplementary material). In Figure 6(a) we compare the number of unlike neighbors at the preferential distance of contact for our one-patch model without flanking-bead patches with different extents of nonadditivity ($\sigma_{CAA} = 1$ and 0.8) and find that softening the cores leads to an increase in the number of neighbors. Note that the minority-component cylinders tend to form two aggregated rows of the minority B particles and have imperfect orientational alignment with observable disclinations. Long disordered tubular structures were also previously found for particles with strong one-patch interaction.³⁰ This anisotropy of the patch NPs favors aggregation between the cores to enable unlike patches to face each other. Our exploration of mixtures of the two-patch NPs (not reported) did not result in phases different from the lamellar phase or disorder cylinders.

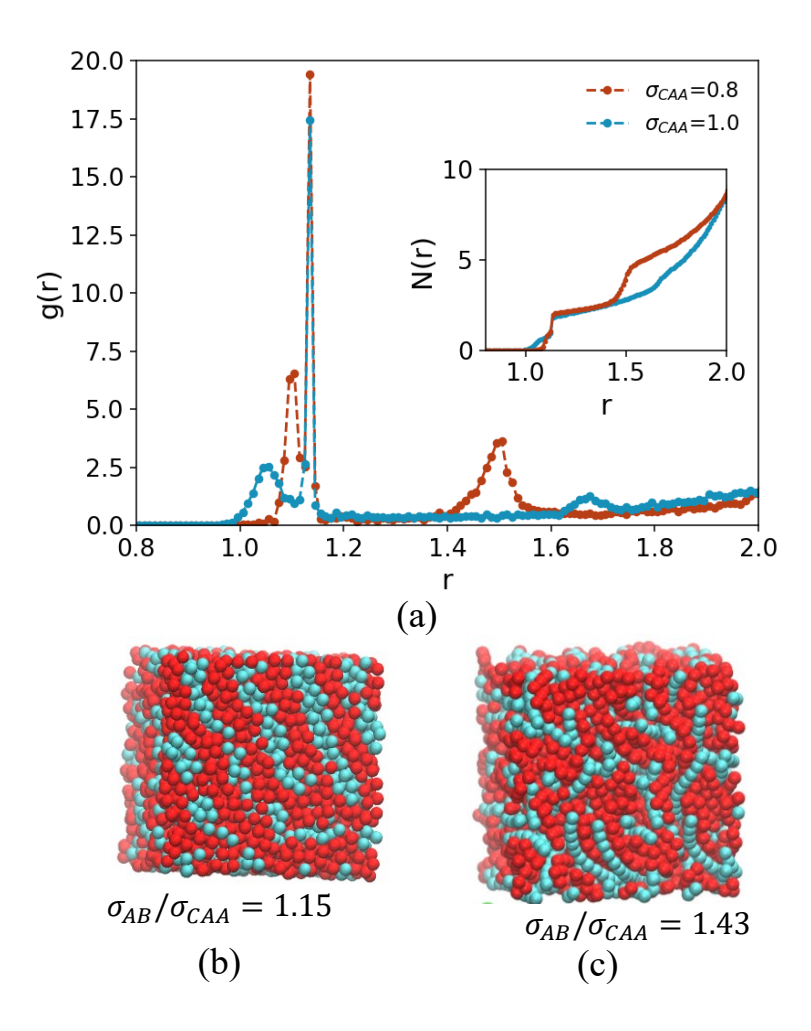


Figure 6: (a) Radial distribution function (g(r)) and coordination number for unlike components (N(r)) for one-patch NPs with $\varepsilon_{PAB}/kT = 3$ and $x_A = 0.66$. Snapshots of the phases formed using (b) $\sigma_{CAA} = 1$ (c) $\sigma_{CAA} = 0.8$.

B. Binary Mixtures of Patchy and (Non-patchy) Spherical Nanoparticles

The mixtures we explored of one-patch NPs with spherical particles also led to lamellar phases regardless of the mole fraction of patchy particles or σ_{CAA} . On the other hand, mixtures containing two-patch NPs exhibited a diverse range of mesophases, depending on the angle between the patches (ϕ) and the two-patch NP mole fraction (x_A) ; only the results for this system are presented

in this section. A summary of the phases formed is compiled in Figure 7, including a peculiar crystalline phase that comprises a two-layer motif, which we denote as the LXY crystal (to be later described in more detail). As was shown in the previous section, layered crystal or lamellar structures are not directly associated with a positive nonadditivity but the presence of patches affects the phase behavior since equimolar mixtures of size-additive spherical particles with preferential attraction tend to assemble into the CsCl lattice instead.²² The remaining phases observed are associated with a minimum level of non-additivity, and the connection between nonadditivity ratios and specific phases will be explored in the following sections. The parameters used to obtain the phases in Figure 7 are compiled in the Supplementary material.

For two-patch NPs as the majority component, gyroidal structures are favored by patch-patch angles near 90°

The primary distinction between a one-patch NP system and a two-patch NP system is that the latter possesses multivalence, which confers the ability to form curved A-B interfaces between particle domains, resulting in a diverse range of phases. Specifically, when the angles between the NP patches fall within the range of $81^{\circ} \le \phi < 109^{\circ}$, the single gyroid phase is observed. To determine this range, we analyzed the structure factor S(k) of the minority component (B) in the formed structures. Figure 8 shows that the characteristic peaks of the gyroid structure factor are lost when ϕ values fall outside the aforementioned range.

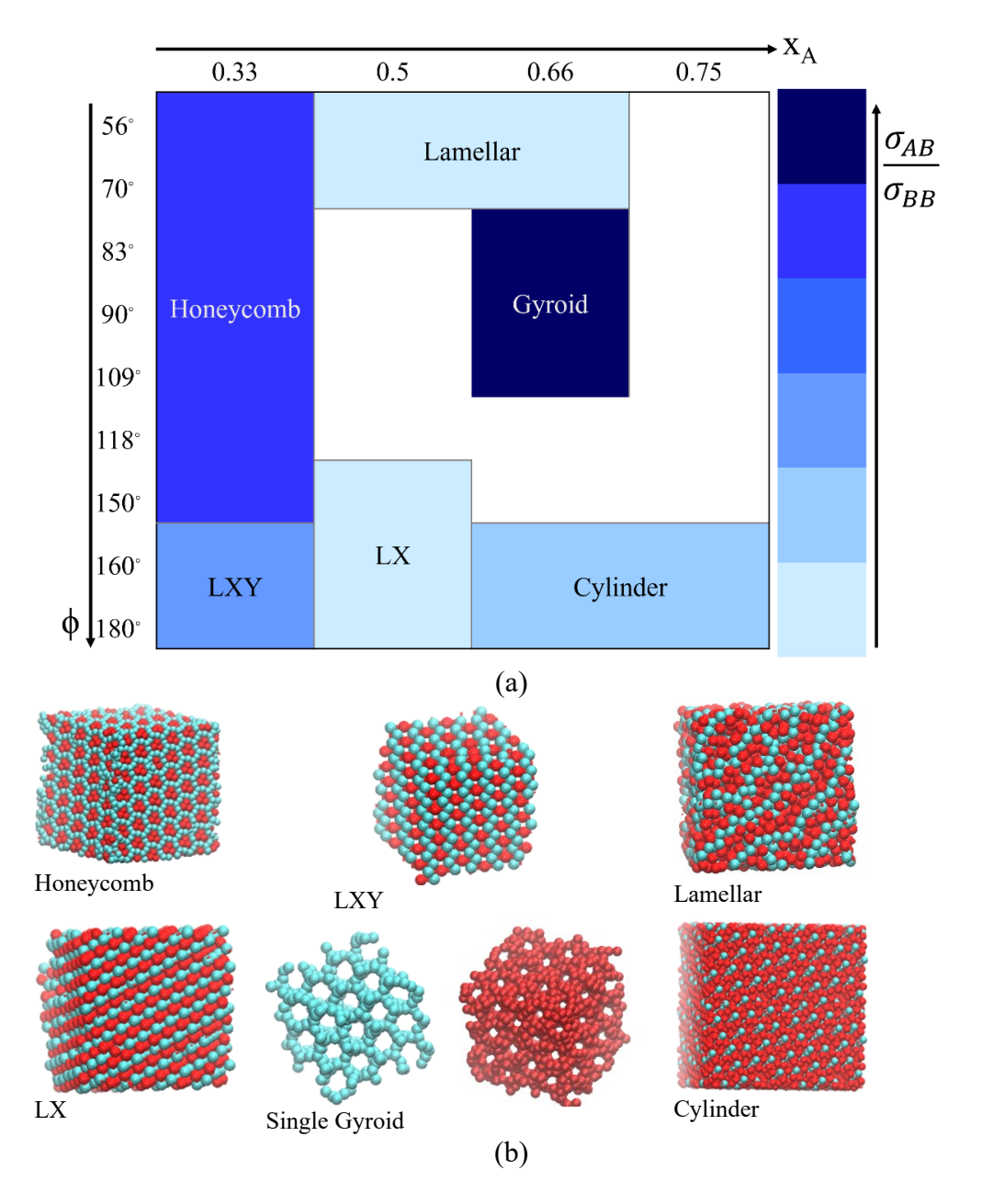


Figure 7: (a) Summary of the main ordered phases formed as a function of the angle ϕ between the two patches of type-A patchy NP (as per Fig. 3(b)), and its molar fraction. (b) Representative snapshots of the different phases. Patchy and spherical NPs are shown in red and cyan,

respectively. In the single gyroid snapshot, the two components are shown separately with the B-type spherical NPs forming the single gyroid network.

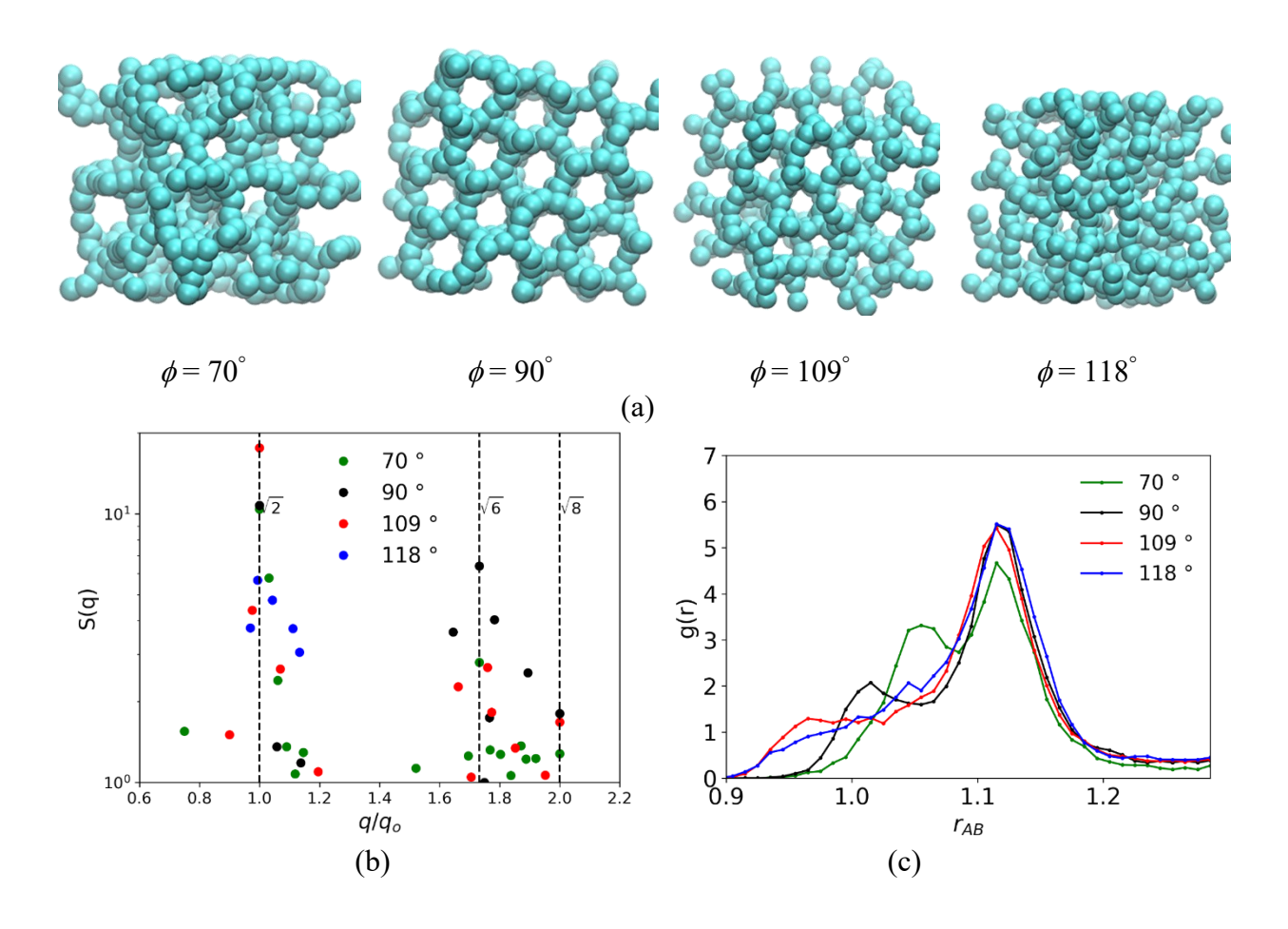


Figure 8: (a) Snapshots of the structure formed by the minority component B in mixtures with type-A two-patch NPs having different angles ϕ between patches. (b) Structure factor of component B for the structures in (a). (c) First-solvation shell of radial distribution function between A-B NPs for different patch angle ϕ (marked in the legend) in A-type NP. Simulation results correspond to x_A = 0.66, σ_{AB} = 1.08, σ_{CAA} = σ_{BB} = 0.7, and ε_{PAB}/kT = 3.

The angular range that favors the gyroidal structure also corresponds to the region in Figure 7 where the potential of mean force (PMF) exhibits two wells. This region is located near $\phi = 90^{\circ}$, where the spherical particle can interact with either one patch or with both patches of the same NP

simultaneously, forming an angle (θ) of approximately 56° between the centers of the spherical particle and the two patches. The presence of these two distinct preferential distances between a spherical NP and the patchy NPs is also evident in the radial distribution function, as depicted in Figure 8 (c), where two peaks are observed at close distances.

For more acute ϕ angles, a smaller θ is more favorable to reduce the repulsive energy associated with any overlap between the patches and the spherical particle. Consequently, in the radial distribution function, the first peak of the distribution for $\phi = 70^{\circ}$ appears at a higher value of r_{AB} compared to that for $\phi = 90^{\circ}$, reflecting the different well positions in the PMFs. On the other hand, obtuse ϕ angles prevent the simultaneous close contact of a single spherical NP with both patches of the same patchy NP, leading to a single peak in the first solvation shell between A and B particles. To further validate these observations, we present the probability distribution of θ angles at the first peak of the radial distribution in Figure 9 (a). A θ color-coded snapshot of the gyroid structure in Figure 9 (b) also shows that most of the particles with $\phi = 90^{\circ}$ have $\theta > 40^{\circ}$ and that there is no significant preference for particles with $\theta < 40^{\circ}$ to be in the node or the strut of the network. The more homogeneous distribution of angles at $\phi = 90^{\circ}$ can be attributed to the strong energetic incentive for particles to be in the second (farther) well position of the corresponding PMF curve, a preference that facilitates the formation of a regular network.

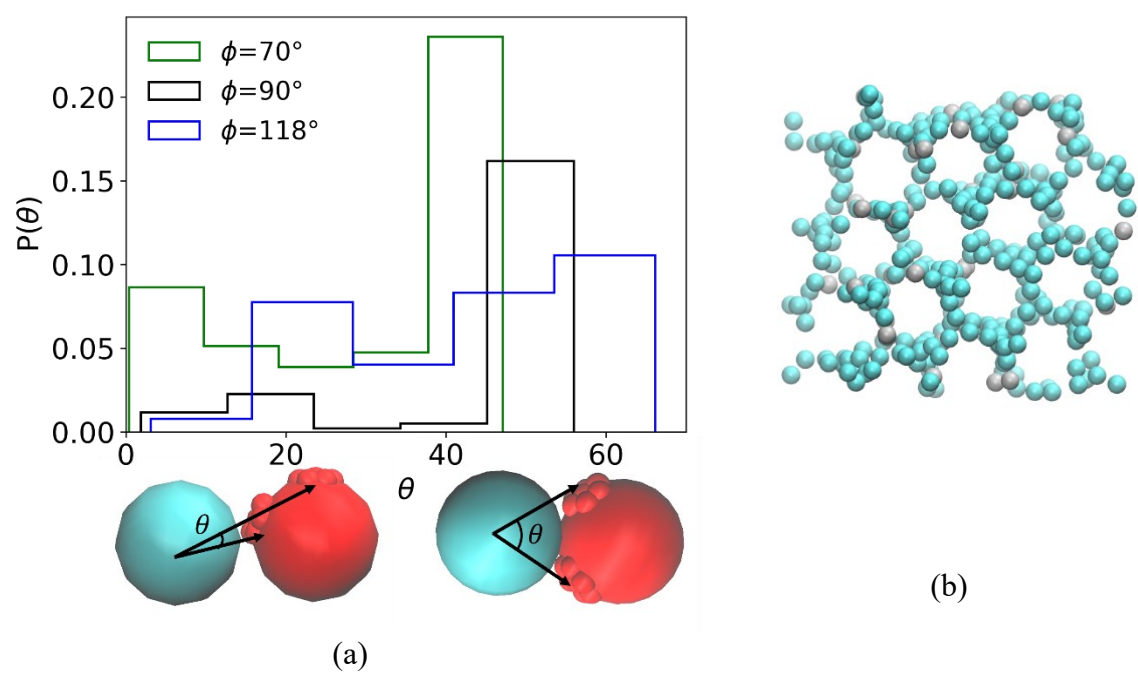
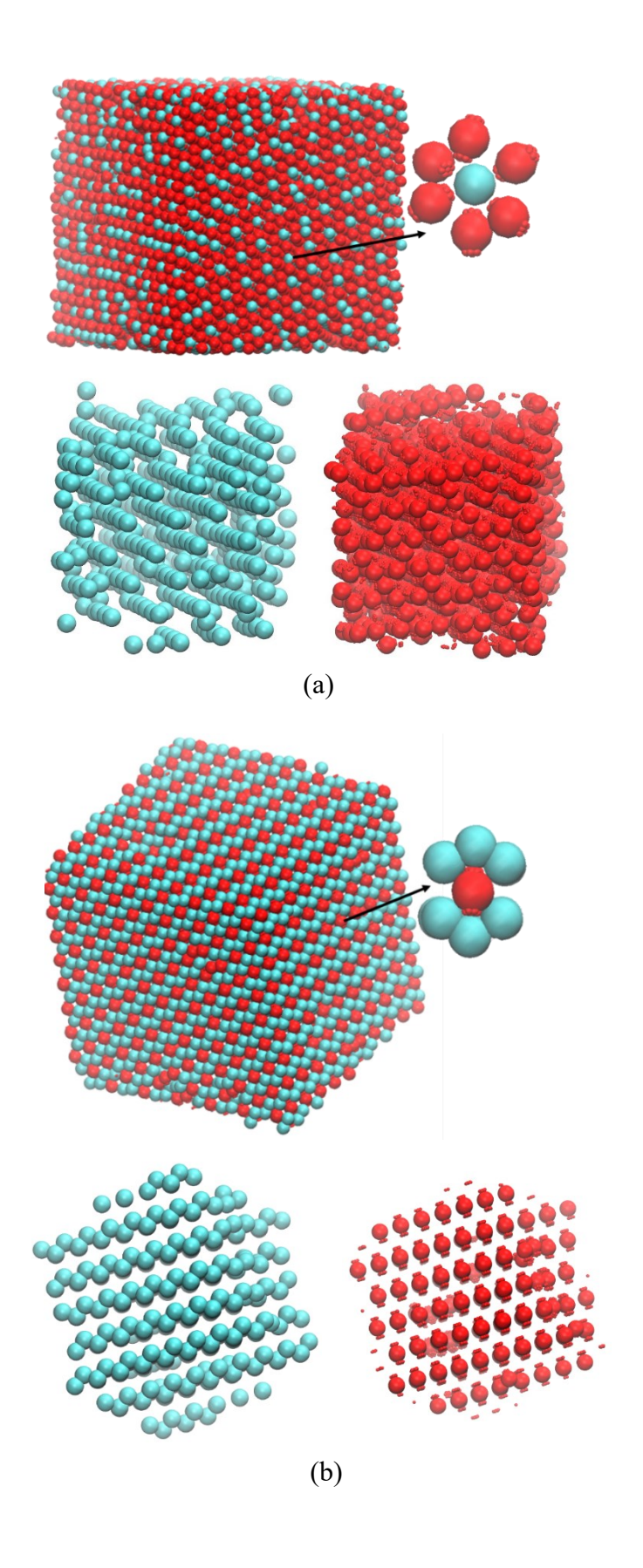


Figure 9: (a) Probability distribution of angle θ between the center of spherical particle B and the patches of particle A at the first peak of the radial distribution from Figure (c). (b) Snapshot of the gyroid structure formed by type-B spherical NPs for $\phi = 90^{\circ}$. B Particles with $\theta > 40^{\circ}/\theta < 40^{\circ}$ are colored in cyan / grey.

When species B is still the minority component but $\phi \ge 155^\circ$, a cylindrical phase forms where the spherical NPs form single-line columns in the characteristic hexagonal lattice, surrounded by 6 patchy NPs (see Fig. 10a). For $115^\circ > \phi > 150^\circ$ the system seems to get trapped in disordered network morphology. The transition between hexagonally packed cylinders and a gyroid phase, mediated by disordered network states, can be understood by the fact that for sufficiently large ϕ , a curvature is induced around the domains of the spherical component B, resulting in tubular structures. Whether such tubes are able to align in a hexagonal pattern or become struts that fuse into nodes in a regular manner, as in the gyroid phase, or in a disordered fashion, is governed by the angle ϕ and the geometric constraints it enacts for A-B contacts.



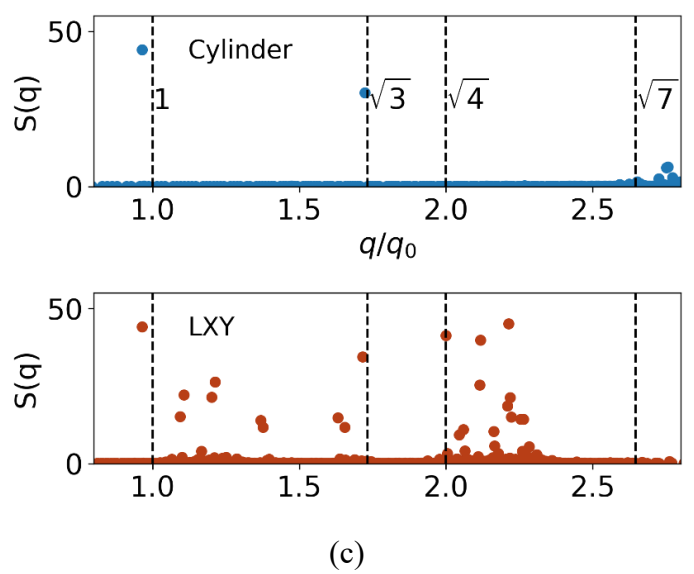


Figure 10: Snapshots and unit cell closeup of (a) the Cylinder phase for x_A = 0.66, and (b) the LXY phase for x_A = 0.33. In (a) and (b) snapshots show the two particle types together (atop) and separately (bottom) with patchy particles (A) colored red and spherical particles (B) cyan. (c) Structure factor of the minority component in the LXY (top) and cylinder (bottom) phases. Simulation results correspond to $\sigma_{AB} = 1.08$ and $\sigma_{CAA} = \sigma_{BB} = 0.8$ for both systems, with $\varepsilon_{PAB}/kT = 3$ for the cylinder phase, and $\varepsilon_{PAB}/kT = 5$ for the LXY phase.

For two-patch NPs as the minority component, a honeycomb phase and a two-layered crystal occur.

When we reverse the relative population of components by making the patchy particles with $150^{\circ} \le \phi \le 56^{\circ}$ the minority component, the gyroid phase is no longer observed; instead, a honeycomb phase is formed. Unlike the gyroid phase, the honeycomb structure can be formed over a wider range of ϕ values. However, acute ϕ angles are associated with a loss of order in both the A and B domains, as observed in the radial distribution function of the honeycomb phase shown in Figure 11.

For $\phi \ge 160^{\circ}$, the mixture assembles into a two-layered crystal (LXY) phase. This phase, whose specific features have not been reported before (to the best of our knowledge), consists of a

crystalline flat layer of species A (patchy NPs) and a zigzagging layer of species B, with regular interstitial gaps, as depicted in Figure 10 (b). In essence, the distance between the patches prevents the simultaneous contact of a patchy NP to the same spherical particle so that favorable energetic contacts are maximized by the local packing/bonding geometry embodied by the LXY phase. In Fig. 10 we contrast the LXY phase structure with the cylindrical phase described earlier which occurs when the A-B composition is reversed (i.e., for patchy NPs as the majority component); while a significant similarity is revealed when seen as "inverse" structures, the key differences are the gaps in the A layers which mediate the appearance of distinct zig-zagging B layers in the LXY structure. Their differences can be quantitatively highlighted by the structure factors of the minority component as shown in Figure 10 (c).

The formation of the LXY phase is preceded by the formation of the lamellar phase as the system is cooled from the isotropic phase. The LXY phase is stabilized for with high energetic attraction strengths between the patches and the spherical NPs ($\varepsilon_{PAB}/kT > 2.4$), while the lamellar phases is associated with weaker strengths ($\varepsilon_{PAB}/kT < 2.4$).

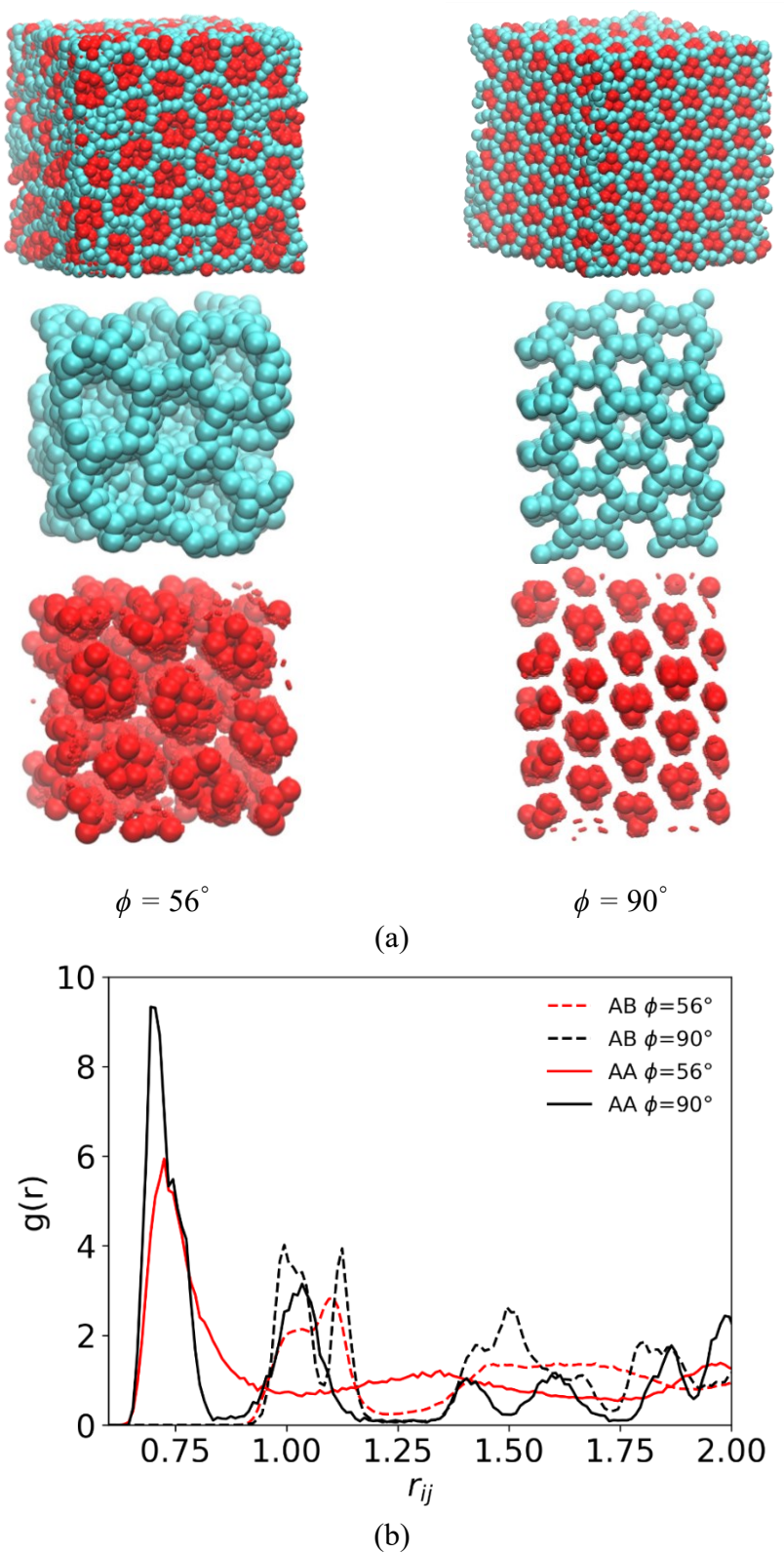


Figure 11: Snapshots of the honeycomb phase formed for different patch-patch angles ϕ . Snapshots show the two particle types together (1st row) and separately (2nd and 3rd row) with

patchy particles (A) colored red and spherical particles (B) cyan. (b) Radial distribution function between particles of types A-B, A-A, B-B for different patch-patch angles (ϕ). Simulation results correspond to $x_A = 0.33$, $\sigma_{AB} = 1.08$, $\sigma_{CAA} = \sigma_{BB} = 0.7$, and $\varepsilon_{PAB}/kT = 3$.

Positive Local Nonadditivity and Phase Formation

With the exception of the lamellar and layered crystal phases, all other phases required positive local nonadditivity values $(\frac{\sigma_{AB}}{\sigma_{BB}} > 1)$, as predicted by our analysis of the Kumar Molinero model. To tune the local nonadditivity, we primarily modified the height of the patch (H) and, consequently, σ_{AB} In order to achieve an even higher level of nonadditivity, we also increased the degree of overlap between the like cores ($\sigma_{CAA} = \sigma_{BB}$), effectively making the like cores softer and shortening their average contact distance. Figure 12 illustrates the relationship between the values of local nonadditivity parameters and the phases observed at temperatures below the orderdisorder transition temperature, $T^* < 1$ (a Table summarizing all the key simulation parameters is provided in the supplementary material). Notably, the gyroid phase required the highest value of nonadditivity. To attain this level, we needed to soften the core by using a minimum of $\sigma_{BB} = 0.8$. For this value of σ_{BB} , decreasing the height of the patch, and consequently, the local nonadditivity, lowered the intensity of the structure factor peaks until the gyroid phase became a disordered network for $\sigma_{AB} = 1.08$. Structure plots and snapshots of the structures for this case are available in the supplementary material. Formation of the honeycomb phase necessitated $\sigma_{BB} \leq 0.9$. Additionally, Figure 12 (c) shows how the particle distances and the assembled phase change with the level of nonadditivity in cases where either a lamellar or a single gyroid phase may form. As discussed in our analysis of the Kumar Molinero model (Table 1), nonadditivity contributes to the microphase segregation associated with mesophase formation by simultaneously maximizing

favorable A-B contacts and minimizing losses in P Δ V and Δ S through increased AA and BB contacts. Contrary to the gyroid phase, the cylinder phase did not require that $\sigma_{BB} < 1$ to form, being able to self-assemble for $\sigma_{BB} = 1$ and a minimum height of the patch of $\sigma_{AB} = 1.10$. We also note in Figure 12 (b) that the formation of the LXY was favored for higher values σ_{AB} , since the flat patch case, $\sigma_{AB} = 1$, required smaller values of σ_{BB} as can be seen in Table S1 of the supplementary material.

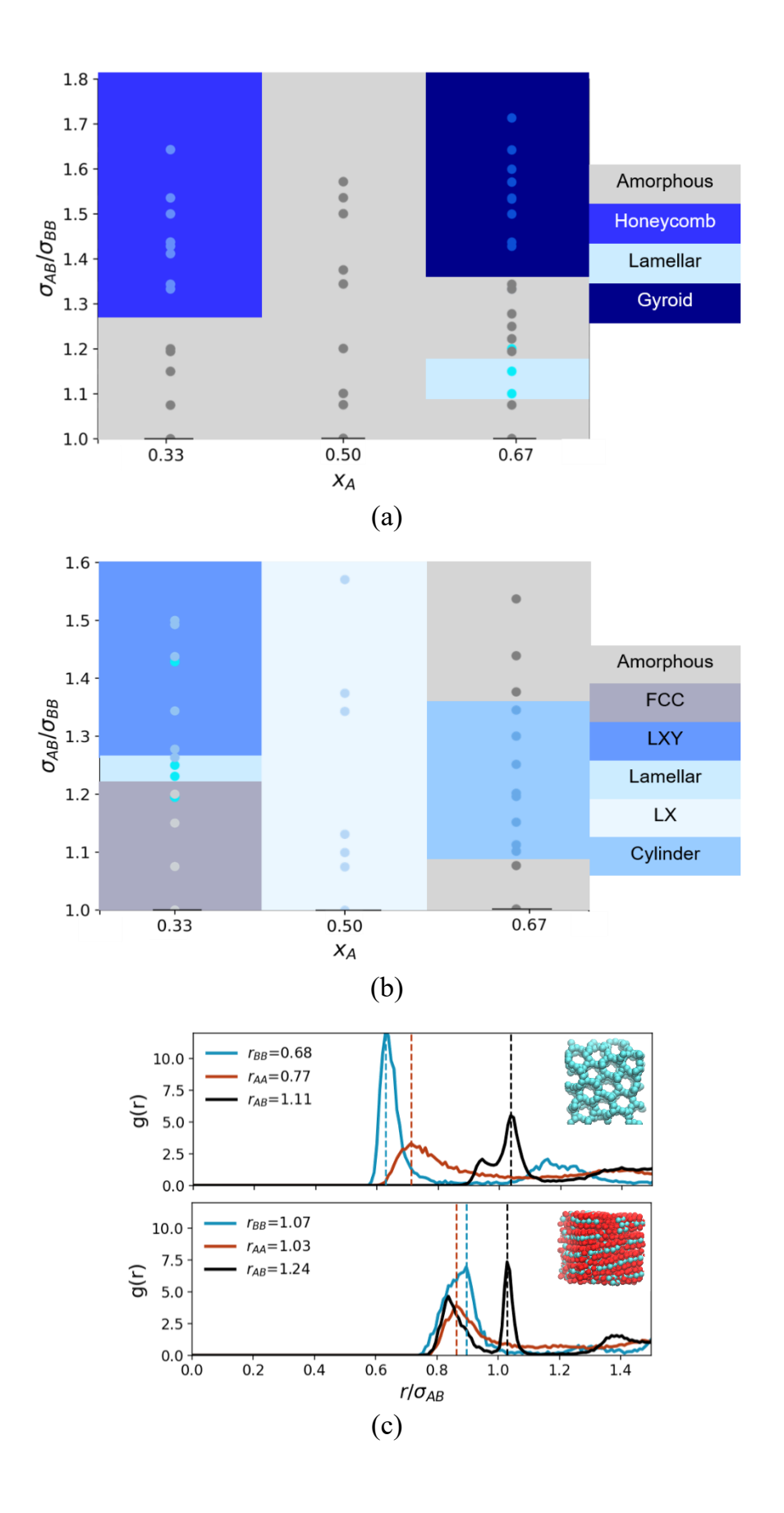


Figure 12: Diagram outlining areas where different phases formed prevalently as a function of the degree of local nonadditivity (σ_{AB}/σ_{BB}) and the fraction of patchy particles (x_A) for: (a) $\phi = 90^{\circ}$ and $\varepsilon_{PAB}/kT = 3.6$, and (b) $\phi = 180^{\circ}$, and $\varepsilon_{PAB}/kT = 5$. Points mark the specific simulation conditions. Points denoted as "amorphous" correspond to states where no clear phase or regular network formed despite some microphase segregation and those denoted as FCC indicate a substitutional disorder FCC phase. (c) Radial distribution function between particles of types A-B, A-A, B-B for the gyroid phase at $\sigma_{AB} = 1.075$, $\sigma_{BB} = 0.7$ (top) and for the lamellar phase at $\sigma_{AB} = 1.2$, $\sigma_{BB} = 1$ (bottom).

IV. CONCLUSIONS

In summary, our study focused on investigating the phase behavior of binary A+B mixtures consisting of spherical NPs decorated with round patches, as well as mixtures of patchy NPs with (non-patchy) spherical NPs. These NPs were designed to have preferential attractions between different species, coarsely simulating the hybridization effect between grafted DNA or DNA-like strands. By raising the patches, a second length scale is introduced to the inter-NP interactions which elicits a local nonadditive behavior that was surmised to potentially lead to the assembly of more complex ordered phases. By adjusting the energetic and geometric parameters of the patches, as well as the softness of core-core interactions, we were able to indeed observe the formation of a variety of mesophases.

Our exploration of the parameter space involved calculating the pair potential of mean force to identify parameters and interaction models that would induce local nonadditivity. We attempted to match the key features of our models with those of the Kumar Molinero (KM) potential model, which exhibits implicit nonadditivity and is known to form mesophases typically associated with block copolymers. Analysis of the KM model revealed that the combination of positive

nonadditivity (relative to the Lorentz mixing rule), the preferential attraction between unlike particles, and the softness of the core-core interactions resulted in a net contraction of the volume in the resulting mesophases (relative to the pre-mixed state of the pure components). Based on this analysis, we investigated the interplay among these factors in our patchy NP model and their correlation with the self-assembly behavior.

In mixtures of one-patch NPs, we probed the effect of local nonadditivity and one-on-one "monovalent" binding between patches. Although we observed various lamellar phases, we did not detect the formation of other mesophases regardless of mixture composition. This preference for lamellar phases suggests that the unidirectional, hard-core interactions strongly favor flat A-B interfaces, leading to lamellar-like morphologies rather than phases with curved A-B interfaces. However, when we softened the interactions, and consequently increased the extent of local nonadditivity, we were able to form cylinder-like phases. This allowed for associations between more than two misaligned patches, resulting in weak "multivalent binding" and curved A-B interfaces. The amount of multivalent binding was quantified by the number of A molecules surrounding one B molecule and vice versa. These cylinder-like phases exhibited some defects and lacked the perfect hexagonal packing symmetry observed in cylinders formed by BCPs and the KM model.

Overall, our results for the raised one-patch model, which provides a physically feasible means of achieving NP nonadditivity, indicate that the directionality and anisotropy introduced by the patches may hinder the formation of network phases. In contrast, the fully isotropic nature of the KM interparticle interactions suggests that some degree of promiscuity or isotropy in the interspecies interactions might be necessary to form the multivalent binding motifs commonly observed in network phases.

To leverage directional interactions and increase the binding valency of NPs, we investigated the use of two-patch particles (A) with different angles between the patches mixed in with spherical particles (B). This mixture exhibited a diverse phase behavior that depended on the angle ϕ between the patches, the fraction of patchy NPs, and the degree of nonadditivity. The phases formed included the gyroid, honeycomb, cylinder, and a two-layered crystal. We demonstrated that a patchy NP with ϕ closer to 90° interacted with spherical particles in such a way that the NP centers and the patch centers did not align but formed an angle that favored the formation of the single gyroid phase. The preference for this angled contact between these A-B particles was related to the shorter range of one of the two potential wells observed in their potential of mean force (PMF). For mixtures with more obtuse patch-patch angles ($\phi \ge 160^{\circ}$), the cylinder phase became favorable as the double well disappeared from the PMF. The formation of non-lamellar or layered phases thus required positive local nonadditivity, with the single gyroid phase requiring the highest extent of nonadditivity.

The strategy of mixing a suitably patchy NPs with spherical NPs can be seen as a promising platform to realize ordered network morphologies out of the spherical NPs. It can be argued that in such systems the patchy NPs acts as a guide (or a structure-directing agent) for the formation of a regular network of spherical soft particles. In this context, once the patchy particles have been created and the suitable ligands identified, spherical particles of varied core chemistries could be equally assembled. These results suggest that these mesophases can be designed to have diverse mechanical, optical, and photonic properties.

The current model can be modified to explore different variants, such as NPs with alternative patch geometries (e.g., rectangular packing instead of hexagonal) and different patch widths. Also importantly, our study was restricted to cases where the A and B components have cores of the

same diameter; core size disparities could open the door to more complex mesophases.

Furthermore, increasing the level of detail by explicitly modeling DNA strands in our patches

could provide insights into additional factors such as chain rigidity and length, which may

influence phase behavior. This will be particularly important when considering "small" NPs (say

with diameters < 30 nm) where the effects of the degrees of freedom of the patch constituents

become more prominent. These questions are the object of our ongoing investigations. While many

new and more refined variants of our models can be explored, our findings already highlight the

importance of targeting nonadditivity when designing and producing NPs capable of mesophase

formation.

Supporting Information

See the supplementary material for additional details provided pertaining to:

(S1) Kumar-Molinero model, (S2) Normalized volume difference, (S3) PMFs for binary mixture

of patchy and spherical nanoparticles model, (S4, S5) one patch particles with flanking beads, (S6)

parameters used in the simulations of binary mixtures of patchy and spherical nanoparticles, (S7)

model details: Base coordinates of patchy particles, (S7) effect of nonadditivity on the structure

factor of network phases. (Supporting Information for Publication.docx)

Corresponding Author

*Fernando A. Escobedo – R. F. Smith School of Chemical and Biomolecular Engineering, Cornell

University, Ithaca, New York, USA; Email: fe13@cornell.edu

34

ACKNOWLEDGMENTS

Funding support from the NSF awards No. CBET-1907369 and CHE-2101829 are gratefully acknowledged. I.Q.M. also acknowledges support from the 2021 MolSSI Fellowship.

Statement of Data Availability:

The data that support the findings of this study are available from the corresponding author upon reasonable request.

REFERENCES

- (1) He, M.; Gales, J. P.; Ducrot, É.; Gong, Z.; Yi, G.-R.; Sacanna, S.; Pine, D. J. Colloidal Diamond. *Nature 2020 585:7826* **2020**, *585* (7826), 524–529. https://doi.org/10.1038/s41586-020-2718-6.
- (2) Kim, Y.-J.; Moon, J.-B.; Hwang, H.; Kim, S.; Yi, G.-R.; Kim, Y.-J.; Moon, J.-B.; Hwang, H.; Kim, Y. S.; Yi, G.-R. Advances in Colloidal Building Blocks: Toward Patchy Colloidal Clusters. *Advanced Materials* **2023**, *35* (4), 2203045. https://doi.org/10.1002/ADMA.202203045.
- (3) Geng, Y.; Van Anders, G.; Dodd, P. M.; Dshemuchadse, J.; Glotzer, S. C. Engineering Entropy for the Inverse Design of Colloidal Crystals from Hard Shapes. *Sci Adv* **2019**, *5* (7), eaaw0514. https://doi.org/10.1126/sciadv.aaw0514.
- (4) Ehlen, A.; Lopez-Rios, H.; Olvera De La Cruz, M. Metallization of Colloidal Crystals. *Phys Rev Mater* **2021**, *5* (11), 115601. https://doi.org/10.1103/PHYSREVMATERIALS.5.115601/FIGURES/9/MEDIUM.
- (5) Marín-Aguilar, S.; Camerin, F.; Dijkstra, M. Guiding the Self-Assembly of Colloidal Diamond. *J Chem Phys* **2022**, *157* (15), 154503. https://doi.org/10.1063/5.0109377.
- (6) Yu, B.; Yang, Q.; Li, H.; Liu, Z.; Huang, X.; Wang, Y.; Chen, H. Gold Nanospirals on Colloidal Gold Nanoparticles. *J Colloid Interface Sci* **2019**, *533*, 304–310. https://doi.org/10.1016/j.jcis.2018.08.065.
- (7) Sacanna, S.; Pine, D. J.; Yi, G.-R. Engineering Shape: The Novel Geometries of Colloidal Self-Assembly. *Soft Matter* **2013**, *9* (34), 8096–8106. https://doi.org/10.1039/C3SM50500F.
- (8) Avendañoa, C.; Jackson, G.; Müller, E. A.; Escobedo, F. A. Assembly of Porous Smectic Structures Formed from Interlocking High-Symmetry Planar Nanorings. *Proc Natl Acad Sci U S A* **2016**, *113* (35), 9699–9703. https://doi.org/10.1073/pnas.1604717113.
- (9) Quintela Matos, I.; Escobedo, F. Congruent Phase Behavior of a Binary Compound Crystal of Colloidal Spheres and Dimpled Cubes. *J Chem Phys* **2020**, *153* (21). https://doi.org/10.1063/5.0030174.
- (10) Karayianni, M.; Pispas, S. Block Copolymer Solution Self-Assembly: Recent Advances, Emerging Trends, and Applications. *Journal of Polymer Science* **2021**, *59* (17), 1874–1898. https://doi.org/10.1002/POL.20210430.

- (11) Dau, H.; Jones, G. R.; Tsogtgerel, E.; Nguyen, D.; Keyes, A.; Liu, Y. S.; Rauf, H.; Ordonez, E.; Puchelle, V.; Basbug Alhan, et al. Linear Block Copolymer Synthesis. *Chem Rev* **2022**, *122* (18), 14471–14553. https://doi.org/10.1021/acs.chemrev.2c00189
- (12) Flavell, W.; Neophytou, A.; Demetriadou, A.; Albrecht, T.; Chakrabarti, D. Programmed Self-Assembly of Single Colloidal Gyroids for Chiral Photonic Crystals. *Advanced Materials* **2023**, 35 (23), 2211197. https://doi.org/10.1002/adma.202211197.
- (13) Whitfield, C. J.; Zhang, M.; Winterwerber, P.; Wu, Y.; Ng, D. Y. W.; Weil, T. Functional DNA-Polymer Conjugates. *Chem Rev* **2021**, *121* (18), 11030–11084. https://doi.org/10.1021/ACS.CHEMREV.0C01074/ASSET/IMAGES/ACS.CHEMREV.0 C01074.SOCIAL.JPEG V03.
- (14) Boles, M. A.; Engel, M.; Talapin, D. V. Self-Assembly of Colloidal Nanocrystals: From Intricate Structures to Functional Materials. *Chem Rev* **2016**, *116* (18), 11220–11289. https://doi.org/10.1021/ACS.CHEMREV.6B00196/ASSET/IMAGES/ACS.CHEMREV.6B00196.SOCIAL.JPEG_V03.
- (15) Rogers, W. B.; Shih, W. M.; Manoharan, V. N. Using DNA to Program the Self-Assembly of Colloidal Nanoparticles and Microparticles. *Nature Reviews Materials 2016 1:3* **2016**, *I* (3), 1–14. https://doi.org/10.1038/natrevmats.2016.8.
- (16) Knorowski, C.; Travesset, A. Self-Assembly and Crystallization of Hairy (f -Star) and DNA-Grafted Nanocubes. *J Am Chem Soc* **2014**, *136* (2), 653–659. https://doi.org/10.1021/ja406241n.
- (17) Wang, S.; Xie, X.; Chen, Z.; Ma, N.; Zhang, X.; Li, K.; Teng, C.; Ke, Y.; Tian, Y. DNA-Grafted 3D Superlattice Self-Assembly. *International Journal of Molecular Sciences* 2021, Vol. 22, Page 7558 2021, 22 (14), 7558. https://doi.org/10.3390/IJMS22147558.
- (18) Wang, S.; Lee, S.; Du, J. S.; Partridge, B. E.; Cheng, H. F.; Zhou, W.; Dravid, V. P.; Lee, B.; Glotzer, S. C.; Mirkin, C. A. The Emergence of Valency in Colloidal Crystals through Electron Equivalents. *Nature Materials* 2022 21:5 2022, 21 (5), 580–587. https://doi.org/10.1038/s41563-021-01170-5.
- (19) Kumar, A.; Molinero, V. Self-Assembly of Mesophases from Nanoparticles. *Journal of Physical Chemistry Letters* **2017**, *8* (20), 5053–5058. https://doi.org/10.1021/acs.jpclett.7b02237.
- (20) Kumar, A.; Molinero, V. Why Is Gyroid More Difficult to Nucleate from Disordered Liquids than Lamellar and Hexagonal Mesophases? *Journal of Physical Chemistry B* **2018**, *122* (17), 4758–4770. https://doi.org/10.1021/acs.jpcb.8b02381.
- (21) Li, Z.; Fan, Q.; Yin, Y. Colloidal Self-Assembly Approaches to Smart Nanostructured Materials. *Chem Rev* **2022**, *122* (5), 4976–5067. https://doi.org/10.1021/acs.chemrev.1c00482.
- (22) Lopez-Godoy, S.; Díaz-Leyva, P.; Kozina, A. Self-Assembly in Binary Mixtures of Spherical Colloids. *Adv Colloid Interface Sci* **2022**, *308*, 102748. https://doi.org/10.1016/J.CIS.2022.102748.
- (23) Knorowski, C.; Burleigh, S.; Travesset, A. Dynamics and Statics of DNA-Programmable Nanoparticle Self-Assembly and Crystallization. *Phys Rev Lett* **2011**, *106* (21), 215501. https://doi.org/10.1103/PhysRevLett.106.215501.
- (24) Condon, J. E.; Jayaraman, A. Effect of Oligonucleic Acid (ONA) Backbone Features on Assembly of ONA-Star Polymer Conjugates: A Coarse-Grained Molecular Simulation Study. *Soft Matter* **2017**, *13* (38), 6770–6783. https://doi.org/10.1039/c7sm01534h.

- (25) Scarlett, R. T.; Ung, M. T.; Crocker, J. C.; Sinno, T. A Mechanistic View of Binary Colloidal Superlattice Formation Using DNA-Directed Interactions. *Soft Matter* **2011**, 7 (5), 1912–1925. https://doi.org/10.1039/c0sm00370k.
- (26) Widom, B.; Rowlinson, J. S. New Model for the Study of Liquid-Vapor Phase Transitions. *J Chem Phys* **1970**, *52* (4), 1670–1684. https://doi.org/10.1063/1.1673203.
- (27) Asakura, S.; Oosawa, F. On Interaction between Two Bodies Immersed in a Solution of Macromolecules. *The Journal of Chemical Physics* **1954**, 22 (7): 1255–1256. https://doi.org/10.1063/1.1740347.
- (28) Holland, B. W. Mixed Localized-Unlocalized Adsorbed Monolayers: Part 2. The Collision Frequency. *Transactions of the Faraday Society* **1965**, *61*, 555–557. https://doi.org/10.1039/TF9656100555.
- (29) Preisler, Z.; Vissers, T.; Smallenburg, F.; Munaò, G.; Sciortino, F. Phase Diagram of One-Patch Colloids Forming Tubes and Lamellae. *Journal of Physical Chemistry B* **2013**, *117* (32), 9540–9547. https://doi.org/10.1021/JP404053T.
- (30) Gianmarco Munaò; Zdenek Preisler; Teun Vissers; Frank Smallenburg; Francesco Sciortino. Cluster Formation in One-Patch Colloids: Low Coverage Results. *Soft Matter* **2013**, *9* (9), 2652–2661. https://doi.org/10.1039/C2SM27490F.
- (31) Rezvantalab, H.; Beltran-Villegas, D. J.; Larson, R. G. Rotator-to-Lamellar Phase Transition in Janus Colloids Driven by Pressure Anisotropy. *Phys Rev Lett* **2016**, *117* (12), 128001. https://doi.org/10.1103/PHYSREVLETT.117.128001.
- (32) Zdeněk Preisler; Teun Vissers; Gianmarco Munaò; Frank Smallenburg; Francesco Sciortino. Equilibrium Phases of One-Patch Colloids with Short-Range Attractions. *Soft Matter* **2014**, *10* (28), 5121–5128. https://doi.org/10.1039/C4SM00505H.
- (33) He, M.; Gales, J. P.; Shen, X.; Kim, M. J.; Pine, D. J. Colloidal Particles with Triangular Patches. *Langmuir* **2021**, *37* (23), 7246–7253. https://doi.org/10.1021/ACS.LANGMUIR.1C00877.
- (34) Neophytou, A.; Chakrabarti, D.; Sciortino, F. Facile Self-Assembly of Colloidal Diamond from Tetrahedral Patchy Particles via Ring Selection. *Proc Natl Acad Sci U S A* **2021**, *118* (48), e2109776118. https://doi.org/10.1073/pnas.2109776118.
- (35) Ho, K. M.; Chan, C. T.; Soukoulis, C. M. Existence of a Photonic Gap in Periodic Dielectric Structures. *Phys Rev Lett* **1990**, *65* (25), 3152. https://doi.org/10.1103/PhysRevLett.65.3152.
- (36) Maldovan, M.; Thomas, E. L. Diamond-Structured Photonic Crystals. *Nature Materials* 2004 3:9 2004, 3 (9), 593–600. https://doi.org/10.1038/nmat1201.
- (37) Quintela Matos, I.; Escobedo, F. A. Influence of Nonadditive Mixing on Colloidal Diamond Phase Formation from Patchy Particles. *J Phys Chem B* **2023**, *127* (16), 3746–3755. https://doi.org/10.1021/acs.jpcb.3c00708.
- (38) Agarwal, U.; Escobedo, F. A. Mesophase Behaviour of Polyhedral Particles. *Nat Mater* **2011**, *10* (3), 230–235. https://doi.org/10.1038/nmat2959.
- (39) Lu, F.; Yager, K. G.; Zhang, Y.; Xin, H.; Gang, O. Superlattices assemblies through shape-induced directional binding, *Nature Comm.* **2015**, *6*, 6921. https://doi.org/10.1038/ncomms7912
- (40) Thompson, A. P.; Aktulga, H. M.; Berger, R.; Bolintineanu, D. S.; Brown, W. M.; Crozier, P. S.; in 't Veld, P. J.; Kohlmeyer, A.; Moore, S. G.; Nguyen, et al. LAMMPS a Flexible Simulation Tool for Particle-Based Materials Modeling at the Atomic, Meso, and

Continuum Scales. *Comput Phys Commun* **2022**, *271*, 108171. https://doi.org/10.1016/J.CPC.2021.108171.

TOC Figure

